CELL BIOLOGY

Live-cell imaging uncovers the relationship between histone acetylation, transcription initiation, and nucleosome mobility

Matthew N. Saxton[1], Tatsuya Morisaki[1], Diego Krapf[2], Hiroshi Kimura[3,4], Timothy J. Stasevich[1,3]*

Histone acetylation and RNA polymerase II phosphorylation are associated with transcriptionally active chromatin, but their spatiotemporal relationship in live cells remains poorly understood. To address this problem, we combine Fab-based labeling of endogenous protein modifications with single-molecule tracking to quantify the dynamics of chromatin enriched with histone H3 lysine-27 acetylation (H3K27ac) and RNA polymerase II serine-5 phosphorylation (RNAP2-Ser5ph). Our analysis reveals that chromatin enriched with these two modifications is generally separate. In these separated sites, we show that the two modifications are inversely correlated with one another on the minutes time scale and that single nucleosomes within each region display distinct and opposing dynamics on the subsecond time scale. While nucleosomes diffuse ~15% faster in chromatin enriched with H3K27ac, they diffuse ~15% slower in chromatin enriched with RNAP2-Ser5ph. These results argue that high levels of H3K27ac and RNAP2-Ser5ph are not often present together at the same place and time, but rather each marks distinct transcriptionally poised or active sites, respectively.

INTRODUCTION

Posttranslational modifications (PTMs) to chromatin and the transcription machinery are tightly coupled during gene activation. Histone H3 acetylation at lysine-27 (H3K27ac), in particular, is strongly correlated with RNA polymerase II serine-5 phosphorylation (RNAP2-Ser5ph), a marker of transcription initiation and pausing at promoters and enhancers (*1*, *2*). A wealth of classic biofractionation, immunoprecipitation, and structural studies has led to a textbook model for how the correlation arises (*3*–*6*). In the model, acetylation neutralizes the positive histone charge and reduces hydrogen bond formation. These processes weaken interactions with negatively charged DNA and other nucleosomes, so individual nucleosomes can move more easily. Acetylation also creates binding substrates for chromatin remodelers and other trans-factors with acetyl-binding domains (*7*). The end result is decondensed, loose, and more mobile chromatin where enhancers and promoters can more easily come into contact and RNAP2 can more easily be recruited and initiated for efficient transcription. Super-resolution imaging of histones in intact, fixed cells further supports this model of chromatin decondensation by histone acetylation (*8*), and numerous genome-wide studies have confirmed acetylation is co-enriched with RNAP2-Ser5ph near gene and enhancer transcription start sites (*2*, *9*).

Although the textbook model provides a clear snapshot of the impact histone acetylation has on chromatin and transcription, the dynamics underlying the model remain poorly understood and have not been validated. This gap arises because PTM dynamics are hard to capture experimentally. Histone acetylation is a dynamic mark whose levels can rapidly change through the fine tuning of the activities of lysine deacetylases (KDACs) and acetyltransferases (KHATs) (*4*, *10*). RNAP2 phosphorylation also rapidly changes as RNAP2 progresses through the various stages of the transcription cycle (*9*, *11*). Resolving the spatiotemporal relationships between highly dynamic acetylation and phosphorylation is therefore especially challenging. Current knowledge of PTM relationships has therefore relied on fixed cell assays, including chromatin immunoprecipitation, immunostaining, and Western blotting. However, in fixed-cell experiments, the dynamics are blurred by the experimental necessity of fixation (which mixes signals in time) and, in many cases, cell population averaging (which mixes signals in space).

To better resolve PTM dynamics, several live-cell imaging techniques have been developed over the last decade. First, we and others have developed technology to directly image and quantify endogenous histone and RNAP2 PTMs in living cells (*12*–*17*). In these studies, fluorescent antibody–based probes are used to rapidly bind and light up residue-specific PTMs in distinct colors. This technology makes it possible to record the temporal fluctuations of the various modifications and better understand their dynamic relationships. Second, individual genetic loci, genes, and nucleosomes can now be tracked in living cells, making it possible to directly measure their mobilities. For example, DNA fluorescence amplification tags can be used to track single genetic loci (*18*–*21*), RNA fluorescence amplification tags can be used to track single-gene transcription (*22*), and both DNA and RNA amplification tags can be combined (*23*–*25*). More recently, advances in single-molecule fluorescence microscopy (*26*, *27*) and fluorescent dye development (*28*) have made it possible to track and quantify the mobility of single nucleosomes (*26*, *29*–*33*). Together, these technologies are revealing a high degree of heterogeneity in chromatin mobility, both within and across cells.

Of the various live-cell imaging studies to date, discrepancies have begun to emerge that raise several fundamental questions about the dynamic relationship between chromatin, gene activation, and histone acetylation. Although there seems to be consensus that dense, constitutive heterochromatin is less mobile than average (*29*,

[1]Department of Biochemistry and Molecular Biology, Colorado State University, Fort Collins, CO, USA. [2]Department of Electrical and Computer Engineering, and School of Biomedical Engineering, Colorado State University, Fort Collins, CO, USA. [3]Cell Biology Center and World Research Hub Initiative, Tokyo Institute of Technology, Yokohama, Japan. [4]School of Life Science and Technology, Tokyo Institute of Technology, Yokohama, Japan.
*Corresponding author. Email: tim.stasevich@colostate.edu

30, 32, 34), the mobility of less dense euchromatin remains debatable. According to the transcription "factory" (35, 36) or "hub" (37) model, transcription sites are thought to be relatively immobile. Here, we refer to transcription factories in a general sense, where transcription factors come together to form a locally concentrated cluster that promotes efficient transcription of one or more nearby genes [as opposed to the more restricted, older definition in which RNAP2 is considered fixed in three-dimensional (3D) space and the fixed complex actively pulls DNA through it]. The clustering of the transcription machinery in factories/hubs is thought to cause nearby chromatin to be constrained or anchored. Recent support for this immobilization comes from several studies that tracked specific genetic loci in living cells and showed that their mobility goes down when associated with transcription (23–25, 38). Additional support comes from single-nucleosome tracking experiments in which a variety of global inhibitors and perturbations of transcription were used to show transcription generally confines single-nucleosome movements (29, 39). Nevertheless, direct imaging of RNAP2 (40) and other components of transcriptional hubs (41, 42) has revealed that they are highly dynamic and transient structures, leaving it questionable to what degree they can immobilize chromatin. Furthermore, some genes and regulatory elements near genes have been observed to become more dynamic upon transcription, providing support for an opposing model whereby transcription "stirs up" chromatin (43), in opposition to the factory/hub concept. Last, the same single-nucleosome tracking studies that showed transcription slows down chromatin also showed generalized acetylation speeds it up (29). These results lead to a paradox: If histone acetylation and transcription initiation act together at the same place and time in the nucleus, as the standard textbook model predicts, then how can active chromatin be both more and less mobile?

Here, we directly confront this conundrum by combining single-molecule tracking (26, 27) with Fab-based imaging of live-endogenous modifications (FabLEM) (12, 13, 15, 44). The combination of these technologies allow us to simultaneously label and directly monitor (i) chromatin dynamics, (ii) transcription initiation (RNAP2-Ser5ph), and (iii) H3K27ac, all without the use of broad-acting inhibitors or perturbations. Using this approach, we show that chromatin enriched with H3K27ac is for the most part physically separated from chromatin enriched with RNAP2-Ser5ph. We furthermore show that the two modifications localize to regions that are oppositely correlated with one another, and the mobilities of nucleosomes therein are substantially different. Together, our data support a model wherein histone acetylation and transcription initiation are enriched in functionally separate chromatin regions with distinct physical behavior.

RESULTS
Global chromatin dynamics are monitored in the context of histone acetylation and RNAP2 phosphorylation
To quantitatively explore the relationship between histone acetylation, RNAP2 phosphorylation, and chromatin dynamics, we first created an RPE1 cell line that stably expresses Halo-tagged histone H2B (H2B-Halo; fig. S1A). With this cell line, we investigated the dynamics of chromatin at multiple time and length scales depending on the concentration of added Halo ligand. At higher concentrations, we could label a substantial fraction of H2B,

allowing us to measure the dynamics of subcellular chromatin regions on the minutes to hours time scale (fig. S1B); at lower concentrations, we could label a tiny subset of H2B, allowing us to measure the dynamics of individual nucleosomes on the subsecond to minutes time scale (fig. S1, C and D).

To place these measurements within the local context of histone acetylation and RNAP2 phosphorylation, we used FabLEM (14) to co-image endogenous H3K27ac—marking active genes and enhancer DNA (45–48)—and endogenous RNAP2 Serine 5 phosphorylation (RNAP2-Ser5ph)—marking transcription initiation sites (11). We were motivated by our previous experiments in which we imaged the same modifications at an artificial tandem gene array activated by the synthetic hormone dexamethasone (13). One of our main findings was that H3K27ac can facilitate gene activation and chromatin decondensation, leading to more efficient RNAP2 recruitment and promoter escape. Because of the artificial nature of the tandem gene array, however, we worried about the generalizability of our findings and wondered whether more natural and less repetitive chromatin would behave the same.

To directly test this hypothesis, we coloaded our stable H2B-Halo cells with the same Fab (fragmented antigen binding regions) we used in the earlier study and performed three-color confocal time lapse microscopy. As illustrated in Fig. 1A, we imaged endogenous H3K27ac using an AF488-conjugated Fab (green), endogenous RNAP2-Ser5ph using a CF640-conjugated Fab (purple), and H2B-Halo using JFX-554-labeled Halo ligand (49) (orange). Unlike standard fluorescent protein fusion tags like green fluorescent protein, which are permanently attached, Fabs only bind their targets transiently. This reduces interference with the underlying biology and allows Fabs to rapidly respond to changes in the posttranslational protein modification landscape (15, 44). To further minimize interference, we kept the concentration of Fab relatively low in cells so target modifications were far from saturated, as we had in our earlier study (13). By imaging cells every 2 to 3 min for 100 time points in total (representing 200 or 300 min, respectively), we generated a complementary pair of datasets that we could mine to precisely quantify the spatiotemporal relationship between H3K27ac and RNAP2-Ser5ph across the entire nucleus (Fig. 1B and movie S1).

To begin to quantify these data in a simple manner, we asked to what degree the H3K27ac and RNAP2-Ser5ph signals were spatially correlated. On the one hand, standard immunoprecipitation assays have long observed a strong positive correlation between histone acetylation and transcription (4, 50). According to this body of work, genes with higher H3K27ac levels should have higher RNAP2-Ser5ph levels (47). On the other hand, immunoprecipitation assays are typically performed in a fixed population of cells, so data represent an average cellular state. Thus, it is unclear whether two modifications are actually present at a single site at the same time in individual cells. For example, it could be feasible that histone acetylation precedes RNAP2 phosphorylation, as we observed at the tandem gene array (13). In this case, the two signals could be spatially anticorrelated at any given time, i.e., they would be spatially segregated.

To test whether our data supported either of these two scenarios, we generated scatterplots from the signal intensities found within the nuclear pixels of all imaged cells. Here, intensity is rescaled from −1 to 1, with $I_{RS} = (I - \langle I \rangle)/(I_{97.5} - I_{2.5})$, where $\langle I \rangle$ is the average intensity and $I_{97.5}$ and $I_{2.5}$ are the 97.5 and 2.5 intensity
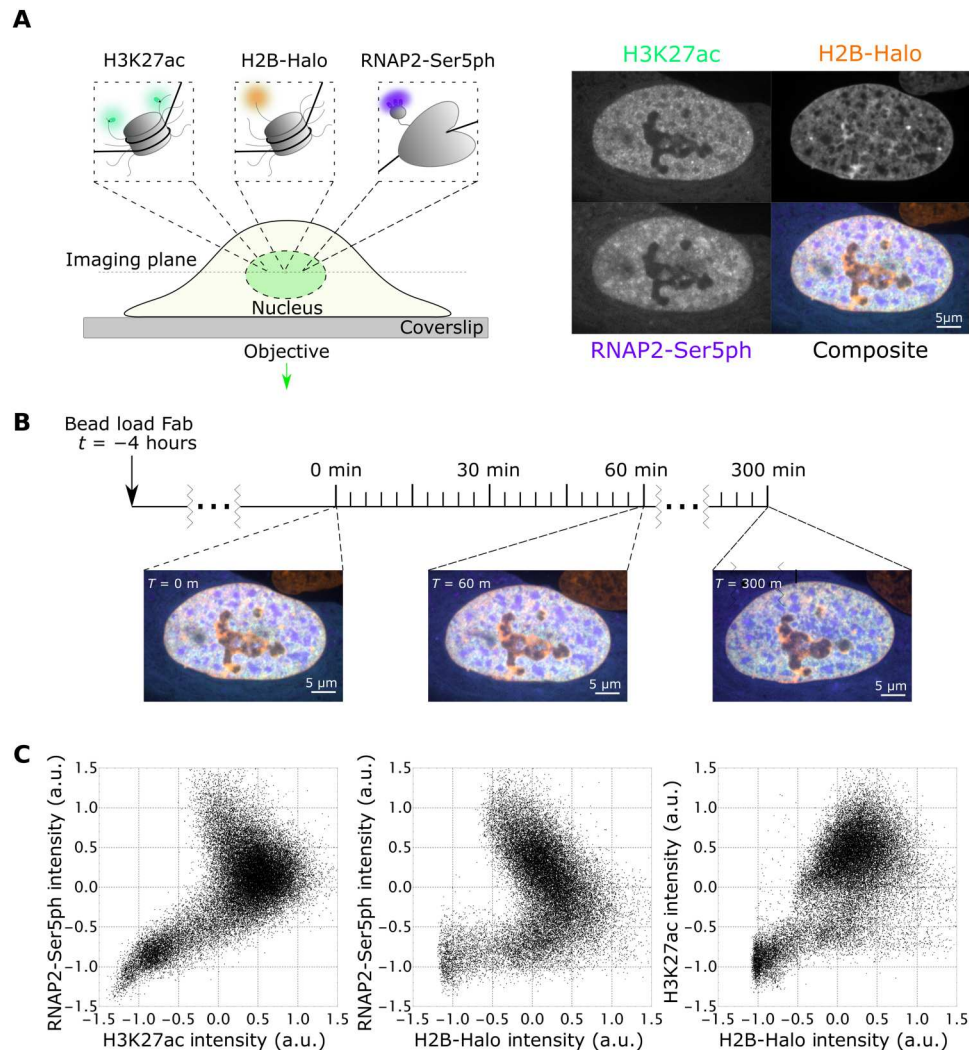
Fig. 1. Simultaneous imaging of RNAP2-Ser5ph, H2B, and H3K27ac in living RPE1 cells. (**A**) Left: Schematic of imaging system. H2B-Halo is stably expressed in RPE1 cells and stained with Halo-JFX-554 ligand. AF488-H3K27ac– and CF640-RNAP2-Ser5ph–specific Fab are bead-loaded into cells, marking each modification in real time. Right: Sample images and composite for all channels. (**B**) Experimental time course. Cells are bead-loaded with Fab 4 hours before imaging, and then H3K27ac, RNAP2-Ser5ph, and H2B channels are collected in a single axial z-plane every 3 min for 300 min. (**C**) Scatterplots of renormalized H3K27ac, RNAP2-Ser5ph, and H2B signal intensities. Each plotted point is the paired intensity values of the same pixel inside of a single nucleus at a single time point, with three representative plots chosen, one for each pairing of channels. a.u., arbitrary units.

quantiles, respectively (Fig. 1C). This analysis revealed a complex relationship between the various signals. For example, while H3K27ac and H2B were overall positively correlated in a fairly linear way (Fig. 1C, right), the relationship between these signals and RNAP2 Ser5ph was more complicated, with clear negative correlation in the upper-right quadrant of the scatterplots where both signals are enriched (Fig. 1C, left and middle). In support of these findings, a full spatial correlation analysis that excluded the nucleoli (where all signals are depleted, i.e., the lower-left region of the scatterplots) clearly shows that H2B and RNAP2 Ser5ph are negatively correlated with one another (fig. S1E). This indicates an overall loss of nucleosomes in transcriptionally active regions. Despite the loss of nucleosomes, however, H3K27ac remains positively correlated with RNAP2, with local maxima in the correlation that peaks at a separation distance of ~2 μm. Together, these data suggest a

complex dynamic between the various signals, with transcriptionally active regions generally depleted in nucleosomes while retaining H3K27 enrichment nearby.

Tracking histone acetylation and RNAP2 phosphorylation dynamics at thousands of endogenous chromatin sites reveals two distinct dynamics

To better assess the complex relationships we saw emerging in our scatterplots and spatial correlation analysis, we next zoomed in on individual chromatin sites to track signals at those sites through time. To achieve this, we created an image processing pipeline consisting of 10 steps (fig. S2A). Briefly, after averaging over five frames and correcting for cell movement (fig. S2, B and C), we used a local adaptive binarization filter to mask, identify, and track thousands of individual chromatin sites that were enriched with either H3K27ac

or RNAP2-Ser5ph (fig. S2, D to F). An example is shown in Fig. 2A, where two individual sites (of many) from a sample cell are tracked through time, the first enriched with H3K27ac (green) and the second enriched with RNAP2-Ser5ph (purple).

In total, we tracked 15,295 nonspecific endogenous chromatin sites spread across the nuclei of 27 cells, 10,290 enriched with H3K27ac, and 5005 enriched with RNAP2-Ser5ph (fig. S3). Consistent with the negative correlation we saw in the upper quadrant of our RNAP2-Ser5Ph versus H3K27ac scatterplot, the two sites tended to border one another but were practically independent, with an overlap that occupied ~5% of the nucleus or less [see, for

example, the combined masks and quantification in fig. S3 (A and B)]. In other words, the data confirmed that regions of chromatin most enriched with H3K27ac had only moderate amounts of RNAP2-Ser5ph and vice versa (fig. S3D).

The sites varied in size, with a median cross-sectional area of $1.12 \pm 0.96 \ \mu m^2$ (SD) for HK27ac-enriched sites and 0.92 ± 0.70 μm^2 (SD) for RNAP2-Ser5ph–enriched sites (fig. S3C). These were too big to be single TADs (51, 52) or clutches (8) but rather more on the order of chromatin territories (53) that would be expected to contain a complex mixture of hundreds of thousands of molecules and PTMs. To get a better feel for their size, note that
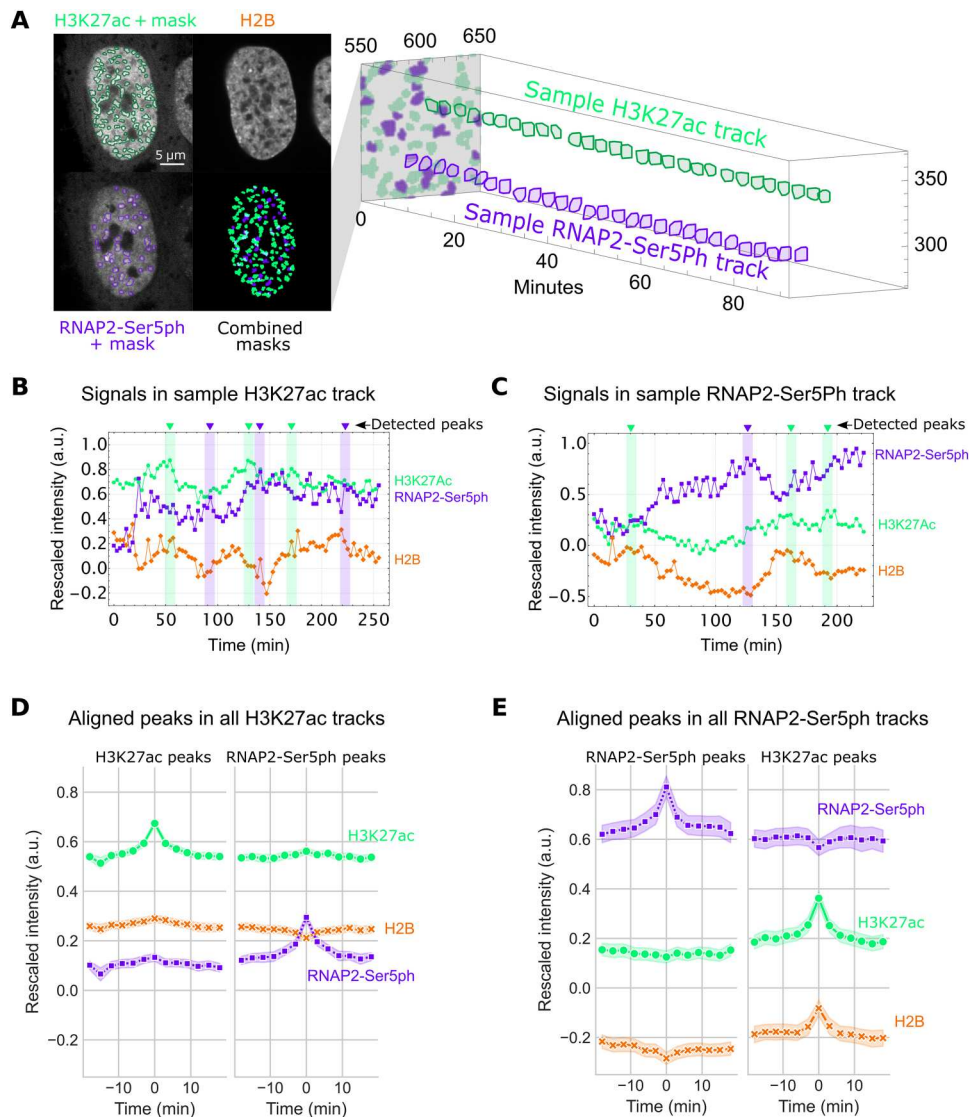
Fig. 2. Hours-long tracking of chromatin regions enriched for H3K27ac and RNAP2-Ser5ph. (**A**) Left: A local adaptive binarization filter is used to identify and isolate regions of chromatin enriched for specific PTMs. Right: Enriched regions are tracked through time. An individual sample of H3K27ac-enriched and RNAP2-Ser5ph–enriched tracks is shown. (**B**) Time traces from a sample track of chromatin enriched for H3K27ac, with average levels of H3K27ac, RNAP2-Ser5ph, and H2B within the region plotted. Identified peaks within H3K27ac and RNAP2-Ser5ph signals are labeled in green and purple, respectively. (**C**) Same as (B), for RNAP2-Ser5ph–enriched region. (**D**) Left: Aligned H3K27ac (n = 2228 peaks) peaks from all H3K27ac-enriched chromatin tracks (n = 10,290 tracks total; n = 2743 greater than 30 frames). All signals were aligned on the basis of the detected peak's time points. Right: Aligned RNAP2-Ser5ph detected peaks (n = 2387) in the same tracks. Error is 95% confidence interval (CI). (**E**) Left: Aligned RNAP2-Ser5ph peaks (n = 874 peaks) from all RNAP2-Ser5ph–enriched chromatin tracks (n = 5005 tracks total; n = 965 greater than 30 frames). All signals were aligned on the basis of the detected peak's time points. Right: Aligned H3K27ac peaks (n = 683) in the same tracks. Error is 95% CI.

each is ~1/200th the volume of a typical nucleus (~200 μm^3). If we assume 60 million nucleosomes per cell, 2% of which harbor H3K27ac (54), then an average site will contain ~300,000 nucleosomes, 6000 of which are acetylated at H3K27ac (corresponding to 12,000 potential H3K27ac sites since each nucleosome contains two H3 molecules). Likewise, if we assume each cell contains ~100,000 initiated RNAP2 (55), then an average site will contain ~500 initiated RNAP2 (corresponding to 26,000 potential Ser5ph sites since each RNAP2 tail contains 52 heptad repeats).

Given the spatially independent nature of chromatin sites enriched with H3K27ac or RNAP2-Ser5ph, we next wondered if the two types of sites displayed different dynamics. To address this question, we quantified the rescaled fluorescence intensities of each track through time (Fig. 2, B and C). Analyzing these tracks in detail revealed a heterogeneous track-to-track population with a number of interesting behaviors and trends. First, many regions of chromatin maintained their enriched status (in either H3K27ac or RNAP2-Ser5ph) for half an hour or longer (see long track lengths in fig. S3C, bottom). When fluctuations did occur inside of H3K27ac-enriched areas, we noticed that all three signals often shifted in sync. However, this was not always the case, as demonstrated by the variability seen in a sample trace (Fig. 2B). Conversely, inside of RNAP2-Ser5ph–enriched chromatin, increases in transcription signal tended to be accompanied by decreases in the H3K27ac and H2B signals and vice versa (Fig. 2C).

To more comprehensively assess generalizable trends, we began by aligning all H3K27ac and RNAP2-Ser5ph signal peaks in both sets of tracks [see small arrows in Fig. 2 (B and C) for a few sample peaks]. We then examined the behavior of all signals when one signal peaked. For example, how H2B and RNAP2-Ser5ph responded when H3K27ac reached a local maximum. As expected, this revealed the dynamics of H3K27ac and RNAP-Ser5ph differed in the two types of sites. In H3K27ac-enriched sites, local peaks in one modification were predictive of faint local peaks in the other modification, whereas in RNAP2-Ser5ph–enriched sites, local peaks in one modification were predictive of small local troughs in the other modification (Fig. 2, D and E). This opposing behavior, while subtle, was consistent across experimental replicates (fig. S4, A and B) and independent of whether we aligned signals by peaks (Fig. 2, D and E, and fig. S4, A and B) or troughs (fig. S4, A and B). While straightforward, examining the behavior of local peaks does not provide a highly quantitative analysis. Thus, we calculated the cross-correlation between the two modifications using signals from all tracks at all time points. As hinted at by our peak alignment results, the cross-correlation demonstrated that the two modifications are positively correlated with one another in sites enriched with H3K27ac but negatively correlated with one another in sites enriched with RNAP2-Ser5ph (fig. S4C).

On the basis of these observations, we can conclude three things. First, the fact that peaks did not always align with peaks (and troughs did not always align with troughs) confirmed that our analysis was free of focus drift or illumination issues that would cause signals to artifactually dim or brighten in sync. Second, despite H2B and H3K27ac being present together within nucleosomes, our peak analysis found that the two signals can be decoupled when acetylation levels are high. Specifically, when we aligned RNAP2-Ser5ph peaks occurring inside highly acetylated tracks, a distinct trough in H2B appeared despite an increase in H3K27ac (Fig. 3D, right). Conversely, when we aligned RNAP2-Ser5ph troughs in the same

tracks, a distinct peak in H2B appeared despite a drop in H3K27ac (fig. S4A, bottom-right). These data therefore provide direct evidence that H3K27ac can act independently of and even counter changes in nucleosome density. Third, the temporal correlation we measured between H3K27ac and RNAP-Ser5ph markedly changed depending on which modification was enriched. When H3K27ac was enriched, the signals fluctuated in a correlated manner, whereas when RNAP2-Ser5ph was enriched, the signals fluctuated in an anticorrelated manner (fig. S4C). We therefore conclude that chromatin enriched with either H3K27ac or RNAP2-Ser5ph displays distinct dynamics from one another on the minutes time scale.
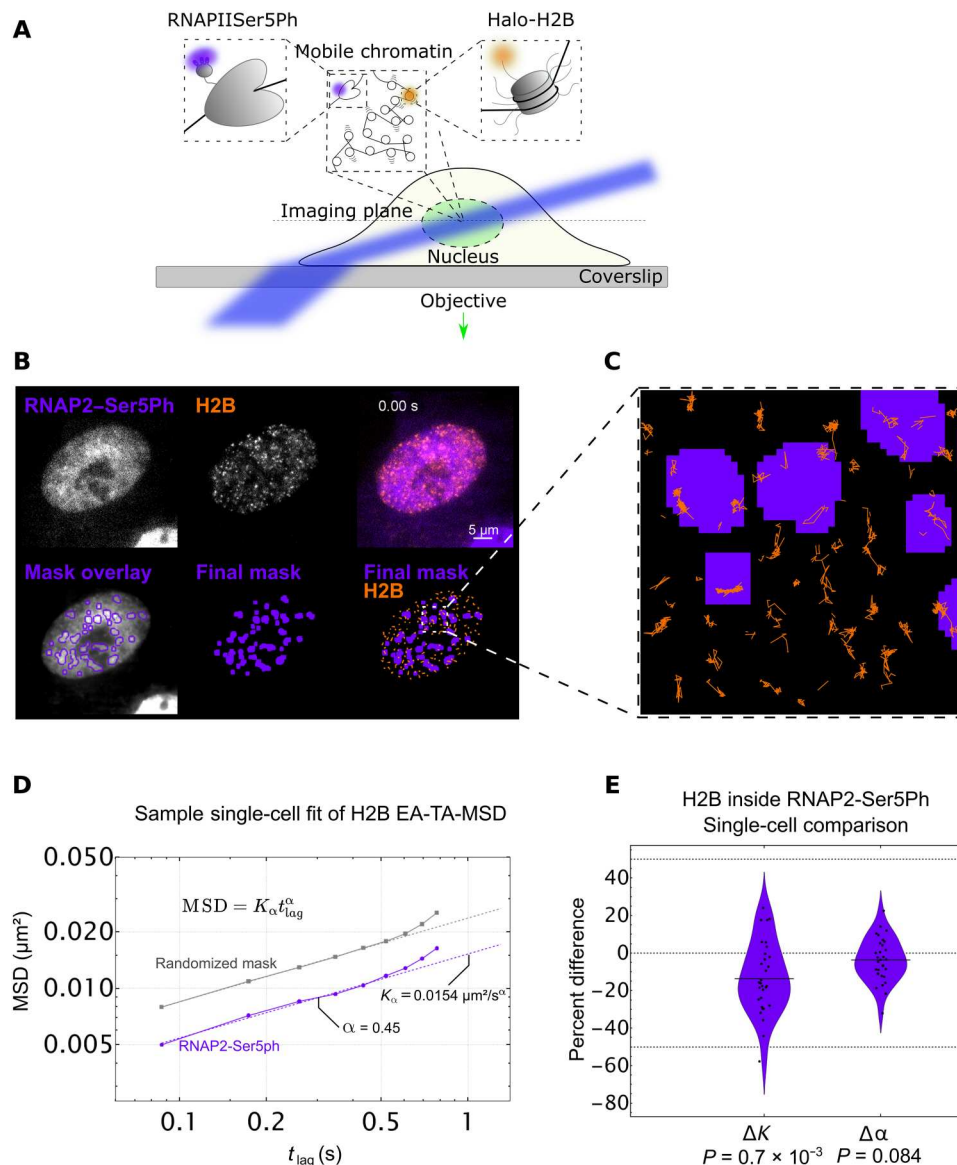
Single-particle tracking of H2B at transcriptionally enriched sites reveals chromatin slowdown

Given the differences in the temporal correlations we observed between sites enriched with H3K27ac and RNAP2-Ser5ph, we were curious whether the two types of sites also exhibited different dynamics on shorter length and time scales. In particular, we wondered whether chromatin within each site exhibited unique microscopic dynamics that could help explain or predict our longer-term observations. Our experimental system was uniquely poised to address this question because we could adjust our imaging setup in a straightforward manner to enable the tracking of individual nucleosomes on the milliseconds time scale while still coimaging PTMs using FabLEM (fig. S1, C and D), and single-particle tracking and the corresponding analysis of trajectories are useful ways to decode the dynamics of intracellular components (56–59).

We first focused on transcriptionally active regions marked by RNAP2-Ser5ph. We hypothesized that nucleosomes in these regions would either diffuse faster or slower than normal. In support of slower nucleosomes, several recent reports (24, 29, 60) have shown an anticorrelative relationship between chromatin mobility and transcriptional activity, consistent with the presence of hypothesized transcription factories or hubs that lock down chromatin (35). In support of faster nucleosomes, on the other hand, it has been observed that some enhancers and promoters are more mobile after differentiation-induced transcription activation in embryonic stem cells, leading to the proposition that RNAP2 transcription activity stirs the local chromatin environment (43).

To see which of these two opposing scenarios is dominant, we again bead-loaded RPE1 cells stably expressing H2B-Halo with AF488-labeled Fab specific to RNAP2-Ser5ph. To enhance fluorescence signal-to-noise and enable long-term tracking of single fluorophores, we switched from confocal to highly inclined laminated optical (HILO) sheet microscopy (Fig. 3A) (27). To acquire many tracks with minimal crossing events, we sparsely labeled H2B-Halo with a reduced form of Tetramethylrhodamine (TMR) ligand that is stochastically photoactivated during imaging (61). Last, we adjusted our imaging rate to a little over 10 frames/s to exclusively track chromatin-incorporated H2B, an indicator for "single nucleosomes" (Fig. 3B and movie S2) (26, 29).

Using this experimental setup, we collected tens of thousands of tracks from 31 cells across three experimental replicates and created an analysis pipeline (fig. S5A). To isolate tracks associated with RNAP2-Ser5ph, we again applied a local adaptive binarization filter to the nuclei of each cell to highlight all subnuclear regions enriched with the specific PTM (Fig. 3B and fig. S5, B and C). We then selected all tracks that remained inside of the mask for at least

Fig. 3. Single-particle tracking of H2B located within transcriptionally active regions marked by RNAP2-Ser5ph. (**A**) Imaging scheme for single-particle H2B tracking experiments using HILO microscopy setup. A combination of H2B-Halo and Fab specific for RNAP2-Ser5ph is used to track single molecules of H2B in the context of transcription. (**B**) Top row, left: Sample single frame of RNAP2-Ser5ph Fab in living RPE1 cells. Middle: Sample single frame of single-molecule H2B-Halo in the same cell. Right: Colored composite of RNAP2-Ser5ph and H2B channels in purple and orange, respectively. Bottom row, left: Outlines of RNAP2-Ser5ph local adaptive binarization mask overlaid upon the 100-frame average image from which the mask was extracted. Middle: Single local adaptive binarization mask of RNAP2-Ser5ph–enriched regions. Right: RNAP2-Ser5ph mask with overlaid H2B-Halo tracks in orange. (**C**) Selected zoom from (B) showing sample full traces of Halo-H2B tracks occurring both inside and outside RNAP2-Ser5ph–enriched regions. (**D**) Sample single-cell fit for the ensemble MSD of all H2B tracks lasting 10 frames or longer, localized in a randomized mask control (gray, n = 5860 total tracks across 10 randomizations) or in RNAP2-Ser5ph–enriched, transcriptionally active regions (purple, n = 463 tracks). Determined diffusion coefficient (K_α) and alpha coefficient (α) for this single-cell fit are labeled, which contributes a single point to (E). Error bars are SEM. (**E**) Difference in K (ΔK) and α ($\Delta\alpha$) for RNAP2-Ser5ph–enriched regions versus a randomized mask control. Each data point represents the difference in fit coefficients for a single-cell fit (n = 31 cells), relative to the mean value, with each cell comprising hundreds to thousands of H2B tracks. Significance determined via Student's t test.

10 consecutive frames (Fig. 3C and fig. S5D). This left us with hundreds to thousands of single-nucleosome tracks per cell to quantify chromatin mobility in the context of RNAP2-Ser5ph.

To ensure that our masking process was not creating a selection bias among our tracks, we created a control mask. For this, we isolated and identified each region of connected pixels in each mask, and each region was then separately moved by a randomized vector.

This procedure created a random mask with a similar morphology to our original mask but randomly dispersed throughout the nucleus (fig. S5, E and F). In so doing, we could compare nucleosome dynamics inside the original RNAP2-Ser5ph mask to average nucleosome dynamics inside a large collection of morphologically identical random masks. This process is critical because restricting tracks to any masked region inherently selects for slower tracks, and

the amplitude of this selection bias depends on the precise size, shape, and morphology of the mask in question (fig. S5G).

To quantitatively compare dynamics in our original and random masks, we fit the ensemble and time-averaged mean-squared displacement (MSD) of nucleosomes to a model of anomalous diffusion (62, 63) such that $MSD = K_\alpha t_{lag}^\alpha$. Here, K_α is the so-called generalized diffusion coefficient, t_{lag} is the lag time or time interval between displacements, and α is the anomalous exponent (Fig. 3D). Similar to other reports (26, 29, 64), our fitted K_α was in the range of 0.03 ± 0.01 μm²/s, while our fitted α was consistently ~0.45 ± 0.1 (even after correcting for both static and dynamic localization errors and eliminating their effect using a resampling approach) (65). Normal diffusion would be characterized by α = 1. In our case, the exponent α indicates that the nucleosomes in the cell nucleus are subdiffusive, i.e., their MSD is sublinear in lag time. The value of fitted α is also very close to the Rouse polymer model expectation of 0.5, consistent with other single-molecule studies of chromatin motion (66–68).

To control for cell-to-cell variability, we subtracted the fitted K_α and α values of nucleosomes inside randomized masks from those inside RNAP2-Ser5ph–enriched masks. This generated a Δα and ΔK for each cell, allowing us to directly compare chromatin dynamics at a single-cell level and controlling for any cell-to-cell variability. As shown in Fig. 3E, the percent change in these differences provided a convenient single-cell measure of the impact RNAP2-Ser5ph enrichment has on single-nucleosome mobilities.

According to our fits, nucleosomes diffusing near chromatin sites enriched with RNAP2-Ser5ph experienced no significant change in the type of diffusion they underwent (Δα ~ 0; Fig. 3E, right). Despite that, the nucleosome diffused ~15% more slowly, characterized by a marked decrease in the diffusion coefficient. This substantial reduction in the mobility of nucleosomes near sites of transcription initiation supports the transcription factory/hub model (35). Furthermore, because our measurements were at random sites in a random set of cells, our data suggest that nucleosome slowdown near transcription initiation is a common event that does not depend on specific perturbations or drug treatments.

Enrichment of H3K27ac predicts an increased nucleosome diffusion

We next turned our attention to histone acetylation, applying the same methodology to chromatin sites enriched with H3K27ac. According to the textbook model, histone acetylation should weaken DNA-nucleosome interactions, theoretically opening up chromatin structure to facilitate nucleosome mobility. In principle, we would therefore predict acetylated nucleosomes have a higher mobility than average. On the other hand, we just observed that less dense, transcriptionally active chromatin can have reduced mobility. The direct relationship between chromatin density and mobility is therefore not obvious. So far, the only study (29) that observed increased single-nucleosome mobility in the context of acetylation relied on the use of trichostatin A (TSA), a broad inhibitor of KDAC proteins that have many nonhistone targets (69). It is therefore unclear how chromatin will behave in regions enriched for H3K27ac.

To more directly address this question, we performed the same experiment as above, except we now loaded cells with AF488-labeled Fab specific for H3K27ac. As before, we tracked single nucleosomes, created real and randomized masks for H3K27ac enrichment, and isolated tracks inside of those regions (Fig. 4, A and B,

and movie S3). We then fit the ensemble and time-averaged MSD from each cell inside the masks to extract K_α and α (Fig. 4C), calculated ΔK and Δα for each cell, and plotted the distributions together (Fig. 4D).

As we saw with RNAP2-Ser5ph, our data indicate that nucleosomes in regions enriched with H3K27ac did not experience any significant change in the type of diffusion they underwent (Δα ~ 0; Fig 4D, right). However, in stark contrast to what we saw with RNAP2-Ser5ph, we now observed a significant increase in the diffusion coefficient K_α. Specifically, our data suggest that nucleosomes diffuse ~15% faster than normal when associated with chromatin enriched for H3K27ac (ΔK > 0; Fig 4D, left). These data therefore provide direct live-cell support that acetylated nucleosomes move more freely in 4D space, as the standard model of histone acetylation would predict. Furthermore, the fact that we observed a speed up in nucleosomes in this case rather than a slow down suggests that our general strategy for measuring nucleosome dynamics in the context of specific PTM masks is unbiased. Together, our data support a model whereby H3K27ac and RNAP2 Ser5ph mark opposing ends of the nucleosome mobility landscape, with H3K27ac marking sites of increased mobility and RNAP2-Ser5ph marking sites of decreased mobility.

DISCUSSION

Despite the well-known correlation between histone acetylation, chromatin structure, and gene activity, the dynamic relationship between these factors has remained largely unexplored in living cells. In this study, we addressed this issue by combining single-molecule tracking with live-cell imaging of PTMs. Using this unique combination of technologies, we quantified the dynamic interplay between endogenous histone acetylation marked by H3K27ac, endogenous transcription initiation marked by RNAP2-Ser5ph, and chromatin mobility marked by stably expressed H2B-Halo.

Our work revealed several fundamental relationships (Fig. 5). First, we showed chromatin that is highly enriched with H3K27ac was generally segregated from chromatin that was highly enriched with RNAP2-Ser5ph. This was a bit unexpected given the strong and positive genome-wide correlation between H3K27ac and RNAP2-Ser5ph regularly observed via chromatin immunoprecipitation. One straightforward explanation for this apparent discrepancy is that individual chromatin sites oscillate between two states, one enriched with H3K27ac and one enriched with RNAP2-Ser5ph. Over time or across a cellular population, this would result in an average coenrichment in signals. Alternatively, a single genetic locus could move back and forth between separate genomic clusters that are enriched with either H3K27ac or RNAP2-Ser5ph. For example, the separate sites could represent distinct clusters of enhancers or distinct clusters of promoters that an individual gene would enter and exit in an oscillatory fashion. Either way, such oscillatory models are not unprecedented as we observed a similar phenomenon at the mouse mammary tumor virus (MMTV) tandem gene array (13). In that study, H3K27ac levels at the array were high before activation, but the levels rapidly dropped postactivation when RNAP2-Ser5ph rapidly rose. Similarly, in another study with zebrafish embryos, high H3K27ac were observed at a developmental gene before its activation, but levels again dropped once RNAP2 was recruited (70). Beyond these specific examples,
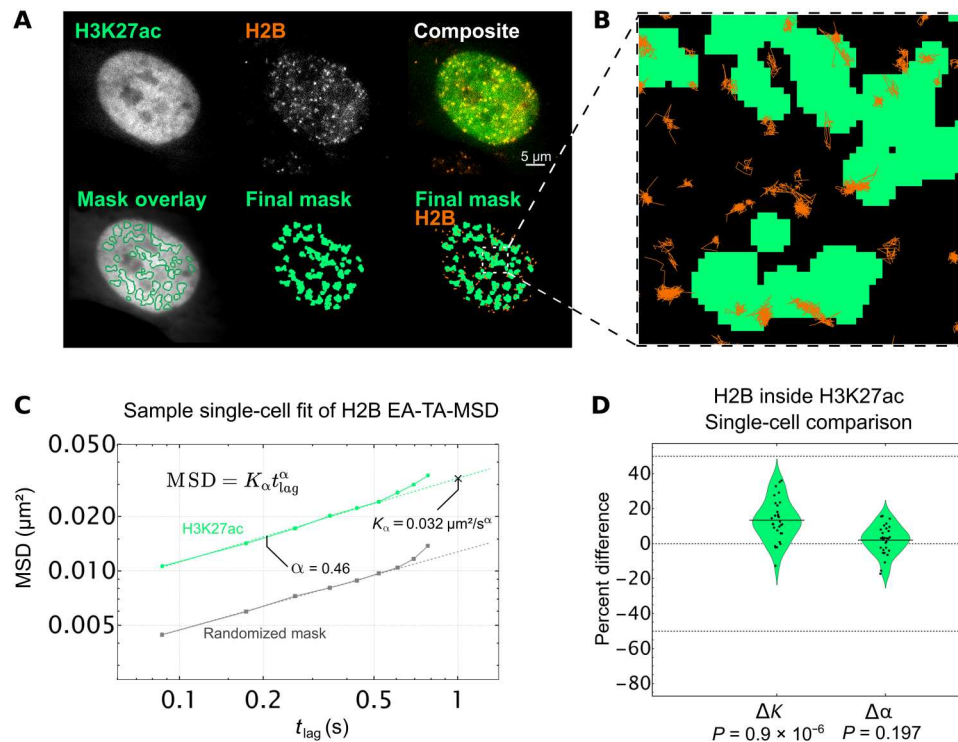
Fig. 4. Single-particle tracking of H2B inside of H3K27ac-enriched chromatin regions. (**A**) Top row, left: Sample single frame of H3K27ac Fab in living RPE1 cells. Middle: Sample single frame of single-molecule Halo-H2B in the same cell. Right: Colored composite of H3K27ac and H2B channels in green and orange, respectively. Bottom row, left: Outlines of H3K27ac local adaptive binarization mask overlaid upon the 100-frame average image from which the mask was extracted. Middle: Single local adaptive binarization mask of H3K27ac-enriched regions. Right: H3K27ac mask with overlaid Halo-H2B tracks in orange. (**B**) Selected zoom from (A) showing sample full traces of Halo-H2B tracks occurring both inside and outside RNAP2-Ser5ph–enriched regions. (**C**) Sample single-cell fit for the ensemble MSD of all H2B tracks lasting 10 frames or longer, localized in a randomized mask control (gray, $n = 1892$ total tracks across 10 randomizations) or in H3K27ac-enriched chromatin (green, $n = 445$ tracks). Determined diffusion coefficient (K_α) and alpha coefficient (α) for this single-cell fit are labeled, which contribute a single point to the violin plot in (D). Error bars are SEM. (**D**) Difference in K (ΔK) and α ($\Delta\alpha$) for RNAP2-Ser5ph–enriched regions from a randomized mask control. Each data point represents the difference in fit coefficients for a single-cell fit ($n = 30$ cells), relative to the mean, with each cell comprising thousands of H2B tracks. Significance determined via Student's t test.

it is now generally accepted that the vast majority of genes display bursty transcription (*71–73*), transitioning between active and inactive states. In light of this, it is tempting to speculate that bursty genes also oscillate between PTM states, having high levels of H3K27ac at one time followed by high levels of RNAP2-Ser5ph at another time. Unfortunately, we were unable to confirm any state transitions in this study because we could only track a specific site while it remained enriched. In the future, this shortcoming could be reconciled by directly labeling and tracking single genetic elements while coimaging H3K27ac and RNAP2-Ser5ph. Among other things, this would allow us to compare the relatively long lifetimes of the sites we tracked with the time scales of individual transcriptional bursts and transcription factor binding.

Second, we showed that the H3K27ac and RNAP2-Ser5ph signals were positively correlated through time in sites enriched with H3K27ac but negatively correlated in sites enriched with RNAP2-Ser5ph. These distinct time-dependent spatial correlations persisted for up to 20 min (fig. S4C), a time scale on par with the transcription cycle of average-sized genes according to RNAP2 fluorescence recovery after photobleaching (FRAP) experiments and bacteriophage MS2-based gene tracking experiments (*74–76*). The data therefore suggest that the relationship between H3K27ac and RNAP2-Ser5ph may change throughout the transcription cycle.

In sites "poised" for transcription (which we define here as high H3K27ac and low RNAP2-Ser5ph), increases in H3K27ac levels help recruit RNAP2 and vice versa (green sites in Fig. 5). On the other hand, in transcriptionally "active" sites (high RNAP2-Ser5ph, lower H3K27ac; purple sites in Fig. 5), increases in H3K27ac lead to a loss in RNAP2-Ser5ph and vice versa, most likely due to enhanced RNAP2 promoter escape or pause release by H3K27ac (*1*, *13*) and the decondensation of nucleosomes by active RNAP2. This dual behavior is consistent with what we observed at the MMTV tandem gene array (*13*). In that study, we showed that H3K27ac at the array before its activation was predictive of (i) the efficiency of transcription factor recruitment immediately after hormone induction and (ii) later RNAP2 promoter escape and chromatin decondensation. Whereas the former would positively correlate with RNAP2-Ser5ph, the latter would negatively correlate. Thus, our data support a model wherein H3K27ac plays multiple roles in tuning gene activation efficiency.

Third, we showed that single nucleosomes diffused ~15% slower than normal in transcriptionally active sites enriched with RNAP2-Ser5ph and ~15% faster than normal in sites enriched with H3K27ac. Together, these data paint a heterogeneous picture of the chromatin mobility landscape (*34*), one that is dynamically colored by local enrichments in specific PTMs (Fig. 5). While the
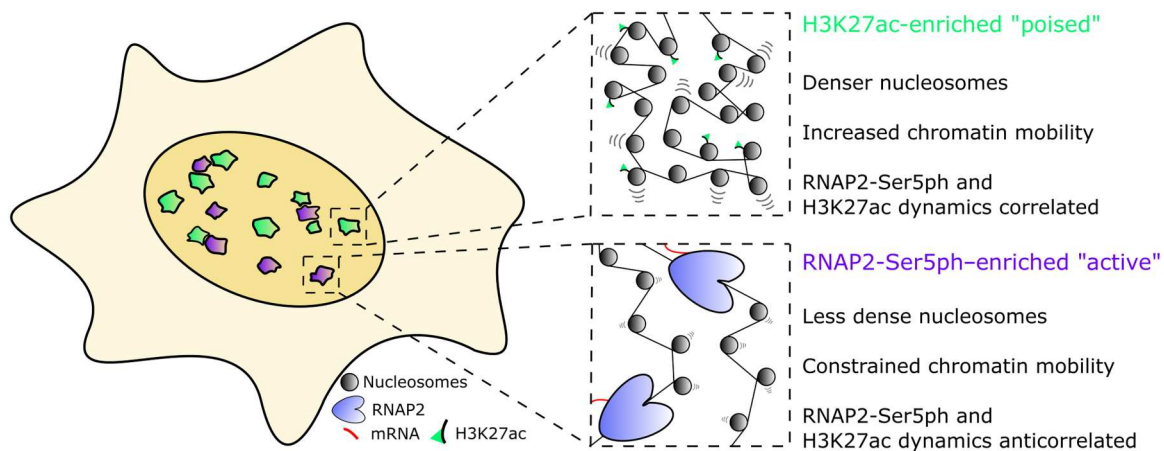
Fig. 5. Two-state model of RNAP2-Ser5ph– and H3K27ac-enriched chromatin domains. Inside the nucleus, two distinct sites are characterized by enrichment for RNAP2-Ser5ph or H3K27ac with little overlap. H3K27ac-enriched regions represent poised chromatin, which is slightly denser than average chromatin but has increased single nucleosome mobility. In combination, these factors reinforce 3D target searching, increasing the probability of contact between genetic elements or interacting proteins. RNAP2-Ser5ph–enriched regions are areas of high transcriptional activity, where chromatin is decondensed but stabilized by the presence of bound transcription machinery.

molecular details of this two-state model have yet to be clarified, it does answer the conundrum between standard model predictions in acetylated and transcriptionally active regions. Namely, H3K27ac and RNAP2 can have separate impacts on chromatin landscape and mobility because they are acting in different places and times in living cells.

Regarding the slowdown of nucleosomes we observed in the context of transcription, our results are consistent with previous reports tracking single-genomic loci (24, 60), as well as with a similar study tracking single nucleosomes in the presence of transcriptional inhibitors (29). Going beyond those previous studies, we have now linked the slowdown to RNAP2-Ser5ph, a specific PTM associated with transcription initiation/pausing (2, 9). Furthermore, we did so without the use of drugs or broad-acting perturbations. Our data therefore support a model wherein transcription initiation is processed predominantly in factories (35) or hubs (41, 42) that tend to lockdown nearby chromatin rather than stir it up (43). While the lockdown we observe is consistent with traditional notions of transcription factories/hubs, we cannot rule out other models of lockdown. For example, crowding within phase-separated condensates (77) or within stiff transcriptional loops (78) could also restrict chromatin mobility. Similarly, we cannot exclude the possibility that some genetic loci behave differently. This is because we had no way of labeling the genomic context of each track. In other words, we could not say if a subset of fast or slow tracks were associated with a specific gene or a specific chromosomal locus. Furthermore, because we focused exclusively on RNAP2-Ser5ph, we may have missed some portion of transcription sites. Recently, there is growing evidence that transcription initiation (marked by RNAP2-Ser5ph) and elongation (marked by RNAP2-Ser2ph) are spatially separated (79, 80). Thus, it is possible that chromatin enriched with actively elongating RNAP2 may still associate with highly mobile nucleosomes (80). In the future, it will therefore be interesting to compare nucleosome mobilities within the context of a wider range of RNAP2 PTMs.

Regarding the enhanced mobility of nucleosomes we observed in the context of H3K27ac, our results are again consistent with a

previous report that tracked nucleosomes in the presence of inhibitors (29). As before, we go beyond this work by directly tracking nucleosomes in the context of a specific PTM without the use of inhibitors, which have many off-target and nonspecific effects. Furthermore, by focusing on the H3K27ac modification, a well-known marker of promoters and enhancers (46), our data suggest that these elements are especially dynamic before transcription activation, in line with the predictions of the standard model of gene activation by histone acetylation. Although we did not examine other residue-specific histone acetylation marks, such as H3K18ac or H3K9ac, we expect many will behave similarly, not only because of the earlier experiments with TSA (29) but also from the classic viewpoint that acetylation acts redundantly to neutralize histone charge (3). In particular, we expect that H3K27ac is most likely redundant because it is written by the promiscuous p300/CBP lysine acetylase subfamily (81), and its complete removal has little impact on fly development and mouse embryonic stem cell differentiation (82, 83). Nevertheless, it will be interesting to examine other acetylations one by one. H3K9, in particular, would be an interesting comparison since it plays a distinct role in nuclear receptor trans-activation and is written independently of H3K27ac by the Gcn5/PCAF lysine acetylase subfamily (84).

In summary, we have combined single-nucleosome tracking with live-cell, multicolor PTM imaging to reveal two types of distinct intranuclear regions that are enriched with RNAP2-Ser5ph or H3K27ac and that display distinct dynamics across multiple time and length scales. We believe that this imaging strategy, combined with computational tools to track, extract, and analyze dynamics within masked regions of cells in an unbiased fashion, create a powerful experimental platform to better elucidate the role residue-specific PTMs play in gene expression networks. The techniques we have developed here can now be used to study a suite of other modifications. For example, beyond acetylation, it will be interesting to mask chromatin marked by other histone PTMs, both individually and in combination. Our methodology to track nucleosomes in the context of PTMs can also be generalized to track other proteins, such as transcription factors or chromatin remodelers. As the

number of PTM-protein combinations is huge, our general method can be broadly applied to help elucidate the hidden roles PTMs play in diverse gene and chromatin regulatory networks.

MATERIALS AND METHODS

Cell culture and care

Human retinal epithelial cells [hTERT-RPE1, American Type Culture Collection (ATCC)] were grown in 10% (v/v) fetal bovine serum (FBS; Atlas)/Dulbecco's modified Eagle's medium (DMEM; Thermo Fisher Scientific). Media was supplemented with 1 mM L-glutamine (Gibco) and 1% (v/v) Penicillin-Streptomycin (Invitrogen/Gibco), and cells were grown at 37°C in 5% CO_2. Cell density was maintained between 15 and 80%. RPE1 cells were purchased from ATCC and were authenticated via short tandem repeat (STR) profiling by ATCC and tested negative for mycoplasma contamination. Cells were stored at −80°C in Cellbanker1 (Amsbio LLC) and thawed >1 week before any imaging.

Stable cell line creation

RPE1 cells were transfected with a Halo-H2B plasmid [constructed as previously described (26)] containing a Neomycin-resistance selection site. Transfection was performed with an LTX Lipofectamine with Plus Reagent kit (Thermo Fisher Scientific), per the manufacturer's instructions. Briefly, an 80% confluency, 35-mm MatTek Chamber was washed, and the media was replaced with 1.75 ml of Opti-MEM (Thermo Fisher Scientific) directly before transfection. The transfection solution included 2.5 μg of DNA plasmid, 7.5 μl of Plus reagent, 7.5 μl of Lipofectamine, and the remainder Opti-MEM for a total solution volume of 250 μl. This solution was incubated for 5 to 15 min at room temperature before being added to the cell chamber. Cells were incubated in this transfection solution for 2 to 4 hours before the media was changed back to 10% FBS-DMEM. Cells were then transferred to a 10-cm dish and allowed to replicate for 14 days under selection at Geneticin G418 Sulfate (750 μg/ml; Gibco). Cells were then stained with Halo-JF646 at 500 nM for 30 min, immediately washed with 1× phosphate-buffered saline (PBS), and sorted via flow cytometry (fluorescence-activated cell sorting) to obtain a consistent population of stable H2B-Halo expressing RPE1 cells. Cells still displayed some heterogeneity in expression, with the brighter cells having signals around four times higher than the dimmer cells. The stable line was maintained under a constant selection of Geneticin (400 μg/ml).

Fab generation and dye conjugation

RNAP2-Ser5ph– and H3K27ac-specific Fab were generated and affinity-purified as previously described (12). Briefly, Fab were generated from monoclonal antibodies using the Pierce Mouse IgG1 Fab and F(ab')2 Preparation Kit (Thermo Fisher Scientific). Antibodies were first digested into Fab in a Zeba Desalt Spin Column (Thermo Fisher Scientific) containing immobilized Ficin while gently rotating for 3 to 5 hours at 37°C. Fab were purified from the digest by centrifugation in a NAb Protein A column. Eluted Fab were concentrated to >1 mg/ml and stored at 4°C. Fab labeling with AF488 and CF640 was performed in small batches using 100 μg of Fab. The dye was an Alexa Fluor 488 ester (Invitrogen) or CF640 (Biotium) dissolved in dimethyl sulfoxide and either used immediately or stored at −20°C. For labeling, 100 μg of Fab was dissolved in a final volume of 100 μl of 100 mM NaHCO₃ (pH 8.5) plus 4 μl of AF488 or 2 μl of CF640 dye. Fabs were incubated with dye for ~2 hours at room temperature with constant gentle rotation and agitation. The Fab were separated from unconjugated dye in an equilibrated PD MiniTrap G-25 desalting column (GE Healthcare). Fab were concentrated in an Amicon Ultra-0.5 Centrifugal Filter Unit (nominal molecular weight limit of 10 kDa; Millipore) to >1 mg/ml. The degree of labeling (DOL) was calculated using the following equation

$$DOL = \left(\frac{\varepsilon_{Fab}}{\varepsilon_{dye}}\right)\left(\frac{1}{(A_{280}/A_{dye}) - CF}\right) \quad (1)$$

ε_{Fab} is the extinction coefficient of Fab (70,000 M^{-1} cm^{-1}), ε_{dye} is the extinction coefficient of the dye used for conjugation (71,000 M^{-1} cm^{-1} for AF488 and 105,000 M^{-1} cm^{-1} for CF640), A_{280} and A_{dye} are the measured absorbances of dye-conjugated Fab fragments at 280 nm and at the peak of the emission spectrum of the dye (488 nm for AF488, 637 nm for CF640), respectively, and CF is the correction factor of the dye (the ratio of the absorbances of the dye alone at 280 nm to at the peak). If the DOL was <0.7, then this protocol was repeated on the same Fab to increase their DOL to ~1. Fab were then stored at 4°C for later use.

Bead loading of Fab and Halo ligand staining before imaging

To bead load RNAP2-Ser5ph– and H3K27ac-specific Fab, cells were plated at ~75% confluency on a 35-mm glass-bottom chamber (MatTek) 24 hours before imaging. Cells were bead-loaded as described previously (85). Briefly, 1.5 μg of each Fab required for an experiment is added together and diluted to 5 μl in 1× PBS. Cell media is removed, and the 5 μl mixture of Fab was pipetted directly on top of the cells, followed by a sprinkling of ~100-μm glass beads to form a monolayer on top of the cells (Sigma-Aldrich). The entire chamber is then lifted and firmly tapped on the worktop six to eight times inside of the culture hood. The media was then immediately replaced, and cells were returned to the incubator. After ~4 hours of recovery, cells were washed three times in phenol-free DMEM with 10% FBS and 1 mM L-glutamine. For single-molecule experiments, HaloTag-TMR ligand was first incubated in 100 mM NaBH₄/1× PBS for 10 min and then diluted to 500 pM, and cells were stained. For non–single-molecule experiments, HaloTag-Janelia-Flour-X554 (JFX554) was used at 200 nM concentration. In all cases, cells were incubated with HaloTag ligand for 30 min and then followed by three times (three washes in DMEM with 10% FBS and 1 mM L-glutamine followed by 5 min of incubation). Cells were moved to the microscope stage-top incubator for imaging ~4 hours postbead loading.

When bead loading RNAP2-Ser5ph– and H3K27ac-specific Fab with this protocol, approximately 10^6 Fab end up in each cell on average (13, 85), less than half of which (~500,000) localize to the cell nucleus. For comparison, approximately 100,000 initiated RNAP2 are phosphorylated at Ser5 in a cell (55). Since each has a heptad repeat that contains 52 potential Ser5ph sites, there are around 5.2 million RNAP2-Ser5ph binding sites per cell. Likewise, there are around 60 million nucleosomes per cell. Since each nucleosome has two H3 tails, there are around 120 million potential H3K27ac sites. Assuming that 2% have the H3K27ac mark (54), then there are around 4.4 million H3K27ac binding sites for Fab per cell. Thus, for both RNAP2-Ser5ph and H3K27ac, we expect the bound fraction of Fab to be fairly low, around 10%.

Live-cell imaging with the confocal microscope

Live-cell images were acquired on an Olympus (IX83) inverted spinning disk confocal microscope equipped with a Cascade II electron multiplying charge-coupled device (EMCCD) camera. A 100× oil immersion objective with a pixel size of 0.096 μm was used for all images. Cells were plated 24 hours before imaging, bead-loaded 4 to 5 hours before imaging, and stained with Halo-JFX554 30 min before imaging, as described above. The chamber was allowed to acclimate in the stage-top incubator for 2 to 3 hours before final image collection to prevent focal shift. The 488-, 561-, and 637-nm lasers were used in all cases. Five frames were acquired in each channel, for each cell, every 2 or 3 min.

Confocal image registration

A sequence of postprocessing functions was applied to all confocal images before any binarization or tracking of specific subnuclear regions. First, for each channel, the five images collected at each time point were averaged together. To correct for cell movement, a maximum intensity projection of all 100 time points of H2B images was created for each cell, and a mask of nucleus movement was drawn by hand around the maximum projection. The mask of nucleus movement was multiplied by all images, leaving only the nucleus of interest. The resultant nuclear H2B images were fed into the FIJI (86) plugin Register Virtual Stack Slices (87), which aligned each nuclear image. This created a list of transformation functions for each time point for each cell, which were then used in conjunction with FIJI plugin Transform Virtual Stack Slices to register the Fab channels for each cell, ensuring that the exact same transformation is applied to all channels.

Identification of subnuclear enriched regions with local adaptive binarization

To isolate subnuclear regions enriched for RNAP2-Ser5Ph or H3K27ac, custom code was written which used a built-in Mathematica function, LocalAdaptiveBinarize. First, a nuclear mask was drawn by hand and multiplied by all images to isolate only the nucleus. Each nuclear image had its intensities normalized from 0 to 1, and a function was applied to each pixel

$$I_{LT} = \alpha \langle I_n \rangle + \beta \sigma_I + \gamma \qquad (2)$$

where I_{LT} is the local threshold, $\langle I_n \rangle$ and σ_I represent the local mean and SD in the neighborhood of n pixels. The values α, β, and γ are user-defined constants. If a pixel's value is higher than the resultant function, then it is set to 1, else it is set to 0. For all masks created, the same parameters were used. These are $n = 441$ (21 × 21 window), α = 0.94, β = 0.6, and γ = 0.05. The resulting binary image had speckle noise eliminated by applying a 10-pixel size filter, and the remaining regions were dilated by 1 pixel to smooth and fill in gaps.

Tracking of RNAP2-Ser5Ph– and H3K27ac-enriched regions

The local adaptive binarization masks from above were then tracked using FIJI plugin TrackMate (88) (v7.6.1) using the following parameters: a Laplacian of Gaussian (LoG) detector; estimated blob diameter: 15.0; pixel threshold: 0.01; subpixel localization: enabled; simple linear assignment problem (LAP) tracker; linking max distance: 10 pixels; gap-closing max distance: 3 pixels; gap-closing max-frame gap: 2 frames. The resulting tracks were fed into custom Mathematica code which finds the region associated

with each x-y coordinate for each track. A region was defined as the set of connected pixels with a value of 1 that are also within 5 pixels in any direction from the X-Y centroid. The values of each channel's raw data pixels (H3K27ac, H2B, and RNAP2-Ser5Ph) were then rescaled for each nuclear image, with −1 and 1 set to the 2.5 and 97.5 quantiles, respectively, to account for outliers. All three channels' pixel intensities within the tracked region were then extracted and averaged together, resulting in a single value for H3K27ac, H2B, and RNAP2-Ser5Ph for each tracked region, for each time point. If the resulting time traces had missing data points due to track gaps, these values were linearly interpolated from adjacent data (less than 3% of total data).

Temporal correlation and cross-correlation analysis

To calculate the correlation of H3K27ac, H2B, and RNAP2-Ser5Ph rescaled intensity traces, the Pearson correlation coefficient was calculated. The mean time-lag cross-correlations were obtained by calculating the Pearson correlation coefficient for each track individually at various time lags and then weighting each time lag by the length of the track used to calculate it. Then, all tracks' cross-correlation curves were averaged. The error of cross-correlation curves was obtained via bootstrapping. To bootstrap, intensity traces were randomly selected from the pool of data, with replacement, equal to the size of the dataset. Then, the mean cross-correlation is calculated as above, and the process is repeated 1000 times. The error is reported as the SD of all 1000 bootstrapped cross-correlation curves.

Peak and trough calling analysis

To find peaks in the H3K27ac and RNAP2-Ser5Ph rescaled intensity tracks, the scipy (89) function in Python scipy.signal.find_-peaks() was used using a "prominence" of 0.15, a "width" of 2, and a "distance" of 10. Troughs were found the same way after signals were inverted. For this analysis, tracks of length < 30 time points were ignored. Also, if peaks were within 10 time points of the beginning or end of a track, then they were ignored (to facilitate easier alignment of all peaks).

Live-cell imaging on the HILO microscope

All live-cell imaging was performed on a custom-built widefield fluorescence microscope with a highly inclined thin illumination scheme described previously. Briefly, the microscope equips three solid-state laser lines (488, 561, and 637 nm from Vortran) for excitation, an objective lens (60×, numerical aperture 1.49 oil immersion, Olympus), an emission image splitter (T660lpxr, ultra-flat imaging grade, Chroma), and two EMCCD cameras (iXon Ultra 888, Andor). Achromatic doublet lenses with 300-mm focal length (AC254-300-A-ML, Thorlabs) were used to focus images onto the camera chips instead of the regular 180-mm Olympus tube lens to satisfy Nyquist sampling (this lens combination produces 100× images with 130 nm/pixel). A single camera was used to capture both Fab (AF488, Thermo Fisher Scientific) and Halo-H2B stained with Halo ligand (TMR, Promega). A high-speed filter wheel (HS-625 HSFW TTL, Finger Lakes Instrumentation) is placed in front of the camera to minimize the bleed-through between the red and the green signals (593/46 nm BrightLine for the red and 510/42 nm BrightLine for the green, Semrock). All single-molecule imaging was performed on a single focal plane for each cell. The laser emission, the camera integration, and the

emission filter wheel position change were synchronized by an Arduino Mega board (Arduino). Image acquisition was performed using open source Micro-Manager software (90) (1.4.22).

Live RPE1 cells were placed into a stage-top environmental chamber at 37°C and 5% CO_2 (Okolab) to equilibrate for at least 30 min before image acquisition. Imaging size and exposure time were set to 256 × 256 pixels and 30 ms, respectively. The resultant imaging rate was ~23 Hz, (43.34 ms per frame). Fab and single-molecule images are alternated, resulting in 86.68 ms per frame for each channel. Laser powers were measured at the back focal plane to be 150 μW for 488 nm and 3.4 mW for 561 nm.

Single-molecule H2B tracking and mask assignment
Single-molecule tracks were identified using TrackMate 5.0.1 (91) with the following parameters: LoG detector; estimated blob diameter: 5.0; pixel threshold: 100; subpixel localization: enabled; simple LAP tracker; linking max distance: 3 pixels; gap-closing max distance: 2 pixels; gap-closing max-frame gap: 1 frame. Movies were 5000 total frames, 2500 of Fab and 2500 of single-molecule H2B in an alternating fashion. Masks were generated by first averaging 100 frames of Fab images and then applying the local adaptive binarization algorithm as above, thereby generating 25 masks which updated every ~8.2 s. Single-molecule H2B tracks were then assigned to a mask based on maximum residence time. Tracks were determined to be inside or outside of H3K27ac, RNAP2-Ser5Ph, or randomized masks based on their subpixel X-Y coordinates. Tracks which crossed between mask borders were split, and track segments which resided in an area for at least 10 consecutive frames were kept.

Diffusion analysis (generating EA-TA-MSD curves, truncating tracks based on length, and fitting for K and α)
TrackMate files were fed into a custom MATLAB script for analysis. To calculate the time-averaged mean square displacement (TAMSD) for each track, all tracks were first truncated to include only their first 10 frames. The rationale for this was to help eliminate any aging bias that may be present in tracks (58). Essentially, as longer times are probed, many particles move out of the single-plane field of view. As a result, probing longer times is vulnerable to biasing the measured trajectories toward the subpopulation that is more subdiffusive or has a smaller diffusion coefficient, simply because they remain within the field of view for the entire time. This bias can be minimized by truncating all tracks to the same length.

TAMSD was calculated as follows (92)

$$\overline{\delta^2(n\Delta t)} = \frac{1}{N-n}\sum_{j=1}^{N-n}\{r[(j+n)\Delta t] - r[j\Delta t]\}^2 \quad (3)$$

where r is xy position as a function of time, the overbar indicates a temporal average, Δt is the frame time, $t_{lag} = n\Delta t$ is the lag time, and N is the number of data points in the trajectory. The ensemble averaged TAMSD (EA-TA-MSD) was calculated by averaging all single-nucleosome TAMSD results for each cell. A localization error of ~30 nm was roughly determined from the intercept of the EA-TA-MSD curve, and a correction was applied to all curves before fitting. To minimize fitting error associated with cell movement (which appears in the MSD curves at time shifts greater than 0.6 s in Figs. 3D and 4C), only the first five points (corresponding to a total time interval of ~0.43 s) of the logarithm of EA-TA-MSD

versus logarithm of time curve for each cell were used in a linear fit to obtain K_α (generalized diffusion coefficient) and α (anomalous exponent) according to

$$\overline{\langle\delta^2(t_{lag})\rangle} \cong K_\alpha t_{lag}^\alpha \quad (4)$$

To obtain ΔK_α and $\Delta\alpha$ for each individual cell, K_α and α obtained using randomized masks were subtracted from K_α and α obtained using the real mask.

Randomized mask generation
A randomized mask was created from the local adaptive binarization of real data through the following process. Each subnuclear component, defined as the series of connected foreground pixels within the local adaptive binarization, had its pixel locations identified. For each component, a randomized vector was created with value between −20 and 20 for both the x and y directions. Each component was then shifted in its entirety by pixels equal to the value of the randomized vector. The result was a randomized, binarized mask that has a morphological nature based on the data from which it was created but with each subnuclear component randomly placed.

Resampling MSD curves to calculate α without static and dynamic errors
MSD data obtained from single-particle tracking are prone to static and dynamics errors, making it challenging to obtain a reliable estimation of the anomaly exponent α (93, 94). To eliminate both types of errors, we use a resampling approach as proposed by Weiss (65). Namely, we analyzed nucleosome trajectories within a real and control mask with minimum lengths 20 or 30 frames. We used two different trajectory lengths to ensure that the approach is robust in terms of number of frames. For each dataset, we resampled the trajectories, taking only even or odd positions, resulting in the two trajectories with frame times $2\Delta t$ for each original one with frame time Δt. The TA-MSD was calculated for the original and resampled data, $\overline{\delta^2(t_{lag})}$. Then, a translated MSD functional is computed for each $v(t_{lag}, \Delta t) = \overline{\delta^2(t_{lag})} - \overline{\delta^2(\Delta t)}$, so that the exponent α is found from the relation

$$v(t_{lag}, 2\Delta t) = 2^\alpha v(t_{lag}, \Delta t) \quad (5)$$

where $v(t_{lag}, 2\Delta t)$ is the functional for the resampled data. The exponent α is thus

$$\alpha = \frac{1}{\log 2}\left\langle\frac{\log[v(t_{lag}, 2\Delta t)]}{\log[v(t_{lag}, \Delta t)]}\right\rangle \quad (6)$$

after averaging over different lag times. The α from three independent datasets were then averaged to find the anomaly exponent for H3K27ac and RNAP2-Ser5ph data and for their associated control masks. For H3K27ac-associated nucleosome tracks, we calculated α = 0.47 ± 0.042 for our real-mask nucleosomes and α = 0.42 ± 0.038 for our control mask nucleosomes. For RNAP2-Ser5ph–associated nucleosome tracks, we calculated α = 0.40 ± 0.062 for our real-mask nucleosomes and α = 0.45 ± 0.075 for our control mask nucleosomes. These values fell into our originally calculated range of α = 0.45 ± 0.1, so while they did not change our conclusions, we performed this analysis to thoroughly rule out any bias from static and dynamic errors.

Spatial auto- and cross-correlation calculations

To calculate the spatial auto- and cross-correlation between signals in fig. S1E, the first frame of all confocal videos was used, with the nucleus and nucleoli masked out using a simple threshold. Once masked, the mean of the image was subtracted so nonmasked signals were evenly distributed about 0. From each channel of this image, the spatial auto- and cross-correlation was calculated using the built-in scipy (89) function scipy.signal.correlate() with mode = "full." The radial average of the resulting correlation image was then calculated by taking the mean of the image in successive rings of width 2 pixels. The correlation as a function of radial distance was then normalized to its value at a radial shift of zero pixels and plotted.

Supplementary Materials

This PDF file includes:
Figs. S1 to S5
Legends for movies S1 to S3

Other Supplementary Material for this manuscript includes the following:
Movies S1 to S3

REFERENCES AND NOTES

1. T. Henriques, B. S. Scruggs, M. O. Inouye, G. W. Muse, L. H. Williams, vBurkholder, C. A. Lavender, D. C. Fargo, K. Adelman Widespread transcriptional pausing and elongation control at enhancers. *Genes Dev.* **32**, 26–41 (2018).

2. L. Core, K. Adelman, Promoter-proximal pausing of RNA polymerase II: A nexus of gene regulation. *Genes Dev.* **33**, 960–982 (2019).

3. P. B. Talbert, S. Henikoff, The Yin and Yang of histone marks in transcription. *Annu. Rev. Genomics Hum. Genet.* **22**, 147–170 (2021).

4. A. L. Clayton, C. A. Hazzalin, L. C. Mahadevan, Enhanced histone acetylation and transcription: A dynamic perspective. *Mol. Cell* **23**, 289–296 (2006).

5. V. G. Allfrey, R. Faulkner, A. E. Mirsky, ACETYLATION AND METHYLATION OF HISTONES AND THEIR POSSIBLE ROLE IN THE REGULATION OF RNA SYNTHESIS. *Proc. Natl. Acad. Sci.* **51**, 786–794 (1964).

6. A. J. Bannister, T. Kouzarides, Regulation of chromatin by histone modifications. *Cell Res.* **21**, 381–395 (2011).

7. G. A. Josling, S. A. Selvarajah, M. Petter, M. F. Duffy, The role of bromodomain proteins in regulating gene expression. *Genes* **3**, 320–343 (2012).

8. J. Otterstrom, A. Castells-Garcia, C. Vicario, P. A. Gomez-Garcia, M. P. Cosma, M. Lakadamyali, Super-resolution microscopy reveals how histone tail acetylation affects DNA compaction within nucleosomes in vivo. *Nucleic Acids Res.* **47**, 8470–8484 (2019).

9. K. M. Harlen, L. S. Churchman, The code and beyond: Transcription regulation by the RNA polymerase II carboxy-terminal domain. *Nat. Rev. Mol. Cell Biol.* **18**, 263–273 (2017).

10. N. T. Crump, C. A. Hazzalin, E. M. Bowers, R. M. Alani, P. A. Cole, L. C. Mahadevan, Dynamic acetylation of all lysine-4 trimethylated histone H3 is evolutionarily conserved and mediated by p300/CBP. *Proc. Natl. Acad. Sci.* **108**, 7814–7819 (2011).

11. M. Heidemann, C. Hintermair, K. Voß, D. Eick, Dynamic phosphorylation patterns of RNA polymerase II CTD during transcription. *Biochim. Biophys. Acta BBA - Gene Regul. Mech.* **1829**, 55–62 (2013).

12. Y. Hayashi-Takanaka, K. Yamagata, T. Wakayama, T. J. Stasevich, T. Kainuma, T. Tsurimoto, M. Tachibana, Y. Shinkai, H. Kurumizaka, N. Nozaki, H. Kimura, Tracking epigenetic histone modifications in single cells using Fab-based live endogenous modification labeling. *Nucleic Acids Res.* **39**, 6475–6488 (2011).

13. T. J. Stasevich, Y. Hayashi-Takanaka, Y. Sato, K. Maehara, Y. Ohkawa, K. Sakata-Sogawa, M. Tokunaga, T. Nagase, N. Nozaki, J. G. McNally, H. Kimura, Regulation of RNA polymerase II activation by histone acetylation in single living cells. *Nature* **516**, 272–275 (2014).

14. H. Kimura, Y. Hayashi-Takanaka, T. J. Stasevich, Y. Sato, Visualizing posttranslational and epigenetic modifications of endogenous proteins in vivo. *Histochem. Cell Biol.* **144**, 101–109 (2015).

15. Y. Sato, M. Nakao, H. Kimura, Live-cell imaging probes to track chromatin modification dynamics. *Microscopy* **70**, 415–422 (2021).

16. S. Conic, D. Desplancq, A. Ferrand, V. Fischer, V. Heyer, B. Reina San Martin, J. Pontabry, M. Oulad-Abdelghani, N. K. Babu, G. D. Wright, N. Molina, E. Weiss, L. Tora, Imaging of native transcription factors and histone phosphorylation at high resolution in live cells. *J. Cell Biol.* **217**, 1537–1552 (2018).

17. S. Conic, D. Desplancq, A. Ferrand, N. Molina, E. Weiss, L. Tora. Visualization of Endogenous Transcription Factors in Single Cells Using an Antibody Electroporation-Based Imaging Approach. in Imaging Gene Expression (ed. Shav-Tal, Y.) vol. 2038 209–221 (Springer New York, 2019).

18. H. Ma, L. C. Tu, A. Naseri, M. Huisman, S. Zhang, D. Grunwald, T. Pederson, Multiplexed labeling of genomic loci with dCas9 and engineered sgRNAs using CRISPRainbow. *Nat. Biotechnol.* **34**, 528–530 (2016).

19. B. Chen, L. A. Gilbert, B. A. Cimini, J. Schnitzbauer, W. Zhang, G. W. Li, J. Park, E. H. Blackburn, J. S. Weissman, L. S. Qi, B. Huang, Dynamic imaging of genomic loci in living human cells by an optimized CRISPR/Cas system. *Cell* **155**, 1479–1491 (2013).

20. I. Tasan, G. Sustackova, L. Zhang, J. Kim, M. Sivaguru, M. HamediRad, Y. Wang, J. Genova, J. Ma, A. S. Belmont, H. Zhao, CRISPR/Cas9-mediated knock-in of an optimized TetO repeat for live cell imaging of endogenous loci. *Nucleic Acids Res.* **46**, e100–e100 (2018).

21. A. F. Straight, A. S. Belmont, C. C. Robinett, A. W. Murray, GFP tagging of budding yeast chromosomes reveals that protein–protein interactions can mediate sister chromatid cohesion. *Curr. Biol.* **6**, 1599–1608 (1996).

22. X. Darzacq, J. Yao, D. R. Larson, S. Z. Causse, L. Bosanac, V. de Turris, V. M. Ruda, T. Lionnet, D. Zenklusen, B. Guglielmi, R. Tjian, R. H. Singer, Imaging transcription in living cells. *Annu. Rev. Biophys.* **38**, 173–196 (2009).

23. T. Germier, S. Audibert, S. Kocanova, D. Lane, K. Bystricky, Real-time imaging of specific genomic loci in eukaryotic cells using the ANCHOR DNA labelling system. *Methods* **142**, 16–23 (2018).

24. H. Ochiai, T. Sugawara, T. Yamamoto, Simultaneous live imaging of the transcription and nuclear position of specific genes. *Nucleic Acids Res.* **43**, e127 (2015).

25. H. Chen, M. Levo, L. Barinov, M. Fujioka, J. B. Jaynes, T. Gregor, Dynamic interplay between enhancer–promoter topology and gene activity. *Nat. Genet.* **50**, 1296–1303 (2018).

26. D. Mazza, A. Abernathy, N. Golob, T. Morisaki, J. G. McNally, A benchmark for chromatin binding measurements in live cells. *Nucleic Acids Res.* **40**, e119–e119 (2012).

27. M. Tokunaga, N. Imamoto, K. Sakata-Sogawa, Highly inclined thin illumination enables clear single-molecule imaging in cells. *Nat. Methods* **5**, 159–161 (2008).

28. J. B. Grimm, B. P. English, J. Chen, J. P. Slaughter, Z. Zhang, A. Revyakin, R. Patel, J. J. Macklin, D. Normanno, R. H. Singer, T. Lionnet, L. D. Lavis, A general method to improve fluorophores for live-cell and single-molecule microscopy. *Nat. Methods* **12**, 244–250 (2015).

29. T. Nozaki, R. Imai, M. Tanbo, R. Nagashima, S. Tamura, T. Tani, Y. Joti, M. Tomita, K. Hibino, M. T. Kanemaki, K. S. Wendt, Y. Okada, T. Nagai, K. Maeshima, Dynamic organization of chromatin domains revealed by super-resolution live-cell imaging. *Mol. Cell* **67**, 282–293.e7 (2017).

30. P. A. Gómez-García, S. Portillo-Ledesma, M. V. Neguembor, M. Pesaresi, W. Oweis, T. Rohrlich, S. Wieser, E. Meshorer, T. Schlick, M. P. Cosma, M. Lakadamyali, Mesoscale modeling and single-nucleosome tracking reveal remodeling of clutch folding and dynamics in stem cell differentiation. *Cell Rep.* **34**, 108614 (2021).

31. S. Hihara, C. G. Pack, K. Kaizu, T. Tani, T. Hanafusa, T. Nozaki, S. Takemoto, T. Yoshimi, H. Yokota, N. Imamoto, Y. Sako, M. Kinjo, K. Takahashi, T. Nagai, K. Maeshima, Local nucleosome dynamics facilitate chromatin accessibility in living mammalian cells. *Cell Rep.* **2**, 1645–1656 (2012).

32. S. Ide, S. Tamura, K. Maeshima, Chromatin behavior in living cells: Lessons from single-nucleosome imaging and tracking. *Bioessays* **44**, e2200043 (2022).

33. M. Lakadamyali, Single nucleosome tracking to study chromatin plasticity. *Curr. Opin. Cell Biol.* **74**, 23–28 (2022).

34. J. Lerner, P. A. Gomez-Garcia, R. L. McCarthy, Z. Liu, M. Lakadamyali, K. S. Zaret, Two-parameter mobility assessments discriminate diverse regulatory factor behaviors in chromatin. *Mol. Cell* **79**, 677–688.e6 (2020).

35. P. R. Cook, A model for all genomes: The role of transcription factories. *J. Mol. Biol.* **395**, 1–10 (2010).

36. P. R. Cook. Principles of Nuclear Structure and Function. (Wiley-Liss, 2001).

37. B. Lim, M. S. Levine, Enhancer-promoter communication: Hubs or loops? *Curr. Opin. Genet. Dev.* **67**, 5–9 (2021).

38. H. Ma, L. C. Tu, Y. C. Chung, A. Naseri, D. Grunwald, S. Zhang, T. Pederson, Cell cycle– and genomic distance–dependent dynamics of a discrete chromosomal region. *J. Cell Biol.* **218**, 1467–1477 (2019).

39. R. Nagashima, K. Hibino, S. S. Ashwin, M. Babokhov, S. Fujishiro, R. Imai, T. Nozaki, S. Tamura, T. Tani, H. Kimura, M. Shribak, M. T. Kanemaki, M. Sasai, K. Maeshima, Single nucleosome imaging reveals loose genome chromatin networks via active RNA polymerase II. *J. Cell Biol.* **218**, 1511–1530 (2019).

40. W.-K. Cho, N. Jayanth, B. P. English, T. Inoue, J. O. Andrews, W. Conway, J. B. Grimm, J. H. Spille, L. D. Lavis, T. Lionnet, I. I. Cisse, RNA Polymerase II cluster dynamics predict mRNA output in living cells. *eLife* **5**, e13617 (2016).

41. W.-K. Cho, J. H. Spille, M. Hecht, C. Lee, C. Li, V. Grube, I. I. Cisse, Mediator and RNA polymerase II clusters associate in transcription-dependent condensates. *Science* **361**, 412–415 (2018).

42. S. Chong, C. Dugast-Darzacq, Z. Liu, P. Dong, G. M. Dailey, C. Cattoglio, A. Heckert, S. Banala, L. Lavis, X. Darzacq, R. Tjian, Imaging dynamic and selective low-complexity domain interactions that control gene transcription. *Science* **361**, (2018).

43. B. Gu, T. Swigut, A. Spencley, M. R. Bauer, M. Chung, T. Meyer, J. Wysocka, Transcription-coupled changes in nuclear mobility of mammalian cis-regulatory elements. *Science* **359**, 1050–1055 (2018).

44. K. Lyon, T. J. Stasevich, Imaging Translational and Post-Translational Gene Regulatory Dynamics in Living Cells with Antibody-Based Probes. *Trends Genet. TIG* **33**, 322–335 (2017).

45. O. Bogdanović, A. Fernandez-Miñán, J. J. Tena, E. de la Calle-Mustienes, C. Hidalgo, I. van Kruysbergen, S. J. van Heeringen, G. J. C. Veenstra, J. L. Gómez-Skarmeta, Dynamics of enhancer chromatin signatures mark the transition from pluripotency to cell specification during embryogenesis. *Genome Res.* **22**, 2043–2053 (2012).

46. M. P. Creyghton, A. W. Cheng, G. G. Welstead, T. Kooistra, B. W. Carey, E. J. Steine, J. Hanna, M. A. Lodato, G. M. Frampton, P. A. Sharp, L. A. Boyer, R. A. Young, R. Jaenisch, Histone H3K27ac separates active from poised enhancers and predicts developmental state. *Proc. Natl. Acad. Sci.* **107**, 21931–21936 (2010).

47. H. Kimura, Histone modifications for human epigenome analysis. *J. Hum. Genet.* **58**, 439–445 (2013).

48. A. Rada-Iglesias, R. Bajpai, T. Swigut, S. A. Brugmann, R. A. Flynn, J. Wysocka, A unique chromatin signature uncovers early developmental enhancers in humans. *Nature* **470**, 279–283 (2011).

49. J. B. Grimm, L. Xie, J. C. Casler, R. Patel, A. N. Tkachuk, N. Falco, H. Choi, J. Lippincott-Schwartz, T. A. Brown, B. S. Glick, Z. Liu, L. D. Lavis, A general method to improve fluorophores using deuterated auxochromes. *JACS Au* **1**, 690–696 (2021).

50. J. H. Shin, R. W. Li, Y. Gao, R. Baldwin, C. Li, Genome-wide ChIP-seq mapping and analysis reveal butyrate-induced acetylation of H3K9 and H3K27 correlated with transcription activity in bovine cells. *Funct. Integr. Genomics* **12**, 119–130 (2012).

51. B. Bintu, L. J. Mateo, J. H. Su, N. A. Sinnott-Armstrong, M. Parker, S. Kinrot, K. Yamaya, A. N. Boettiger, X. Zhuang, Super-resolution chromatin tracing reveals domains and co-operative interactions in single cells. *Science* **362**, (2018).

52. Q. Szabo, F. Bantignies, G. Cavalli, Principles of genome folding into topologically associating domains. *Sci. Adv.* **5**, eaaw1668 (2019).

53. J. C. Hansen, K. Maeshima, M. J. Hendzel, The solid and liquid states of chromatin. *Epigenetics Chromatin* **14**, 50 (2021).

54. G. LeRoy, P. A. DiMaggio, E. Y. Chan, B. M. Zee, M. A. Blanco, B. Bryant, I. Z. Flaniken, S. Liu, Y. Kang, P. Trojer, B. A. Garcia, A quantitative atlas of histone modification signatures from human cancer cells. *Epigenetics Chromatin* **6**, 20 (2013).

55. H. Kimura, Y. Tao, R. G. Roeder, P. R. Cook, Quantitation of RNA polymerase II and its transcription factors in an HeLa cell: Little soluble holoenzyme but significant amounts of polymerases attached to the nuclear substructure. *Mol. Cell. Biol.* **19**, 5383–5392 (1999).

56. C. Manzo, M. F. Garcia-Parajo, A review of progress in single particle tracking: From methods to biophysical insights. *Rep. Prog. Phys.* **78**, 124601 (2015).

57. H. Shen, L. J. Tauzin, R. Baiyasi, W. Wang, N. Moringo, B. Shuang, C. F. Landes, Single particle tracking: From theory to biophysical applications. *Chem. Rev.* **117**, 7331–7376 (2017).

58. A. Sabri, X. Xu, D. Krapf, M. Weiss, Elucidating the origin of heterogeneous anomalous diffusion in the cytoplasm of mammalian cells. *Phys. Rev. Lett.* **125**, 058101 (2020).

59. G. Muñoz-Gil, G. Volpe, M. A. Garcia-March, E. Aghion, A. Argun, C. B. Hong, T. Bland, S. Bo, J. A. Conejero, N. Firbas, Ò. Gariboi Orts, A. Gentili, Z. Huang, J. H. Jeon, H. Kabbech, Y. Kim, P. Kowalek, D. Krapf, H. Loch-Olszewska, M. A. Lomholt, J. B. Masson, P. G. Meyer, S. Park, B. Requena, I. Smal, T. Song, J. Szwabiński, S. Thapa, H. Verdier, G. Volpe, A. Widera, M. Lewenstein, R. Metzler, C. Manzo, Objective comparison of methods to decode anomalous diffusion. *Nat. Commun.* **12**, 6253 (2021).

60. T. Germier, S. Kocanova, N. Walther, A. Bancaud, H. A. Shaban, H. Sellou, A. Z. Politi, J. Ellenberg, F. Gallardo, K. Bystricky, Real-time imaging of a single gene reveals transcription-initiated local confinement. *Biophys. J.* **113**, 1383–1394 (2017).

61. L. Carlini, A. Benke, L. Reymond, G. Lukinavičius, S. Manley, Reduced dyes enhance single-molecule localization density for live superresolution imaging. *ChemPhysChem* **15**, 750–755 (2014).

62. R. Metzler, J.-H. Jeon, A. G. Cherstvy, E. Barkai, Anomalous diffusion models and their properties: Non-stationarity, non-ergodicity, and ageing at the centenary of single particle tracking. *Phys. Chem. Chem. Phys.* **16**, 24128–24164 (2014).

63. D. Krapf Chapter Five - Mechanisms Underlying Anomalous Diffusion in the Plasma Membrane. in Current Topics in Membranes (ed. Kenworthy, A. K.) vol. 75 167–207 (Academic Press, 2015).

64. G. A. Lovely. Direct observation of RAG recombinase recruitment to chromatin and the IgH locus in live pro-B cells. 2020.09.07.286484 Preprint at https://doi.org/10.1101/2020.09.07.286484 (2020).

65. M. Weiss, Resampling single-particle tracking data eliminates localization errors and reveals proper diffusion anomalies. *Phys. Rev. E* **100**, 042125 (2019).

66. M. Gabriele, H. B. Brandão, S. Grosse-Holz, A. Jha, G. M. Dailey, C. Cattoglio, T. H. S. Hsieh, L. Mirny, C. Zechner, A. S. Hansen, Dynamics of CTCF- and cohesin-mediated chromatin looping revealed by live-cell imaging. *Science* **376**, 496–501 (2022).

67. P. Mach, P. I. Kos, Y. Zhan, J. Cramard, S. Gaudin, J. Tünnermann, E. Marchi, J. Eglinger, J. Zuin, M. Kryzhanovska, S. Smallwood, L. Gelman, G. Roth, E. P. Nora, G. Tiana, L. Giorgetti, Cohesin and CTCF control the dynamics of chromosome folding. *Nat. Genet.* **54**, 1907–1918 (2022).

68. V. I. P. Keizer, S. Grosse-Holz, M. Woringer, L. Zambon, K. Aizel, M. Bongaerts, F. Delille, L. Kolar-Znika, V. F. Scolari, S. Hoffmann, E. J. Banigan, L. A. Mirny, M. Dahan, D. Fachinetti, A. Coulon, Live-cell micromanipulation of a genomic locus reveals interphase chromatin mechanics. *Science* **377**, 489–495 (2022).

69. M. A. Glozak, N. Sengupta, X. Zhang, E. Seto, Acetylation and deacetylation of non-histone proteins. *Gene* **363**, 15–23 (2005).

70. Y. Sato, L. Hilbert, H. Oda, Y. Wan, J. M. Heddleston, T. L. Chew, V. Zaburdaev, P. Keller, T. Lionnet, N. Vastenhouw, H. Kimura, Histone H3K27 acetylation precedes active transcription during zebrafish zygotic genome activation as revealed by live-cell analysis. *Development* **146**, dev179127 (2019).

71. T. L. Lenstra, J. Rodriguez, H. Chen, D. R. Larson, Transcription dynamics in living cells. *Annu. Rev. Biophys.* **45**, 25–47 (2016).

72. A. Raj, C. S. Peskin, D. Tranchina, D. Y. Vargas, S. Tyagi, Stochastic mRNA synthesis in mammalian cells. *PLoS Biol.* **4**, e309 (2006).

73. Z. S. Singer, J. Yong, J. Tischler, J. A. Hackett, A. Altinok, M. A. Surani, L. Cai, M. B. Elowitz, Dynamic heterogeneity and DNA methylation in embryonic stem cells. *Mol. Cell* **55**, 319–331 (2014).

74. L. S. Forero-Quintero, W. Raymond, T. Handa, M. N. Saxton, T. Morisaki, H. Kimura, E. Bertrand, B. Munsky, T. J. Stasevich, Live-cell imaging reveals the spatiotemporal organization of endogenous RNA polymerase II phosphorylation at a single gene. *Nat. Commun.* **12**, 3158 (2021).

75. X. Darzacq, Y. Shav-Tal, V. de Turris, Y. Brody, S. M. Shenoy, R. D. Phair, R. H. Singer, In vivo dynamics of RNA polymerase II transcription. *Nat. Struct. Mol. Biol.* **14**, 796–806 (2007).

76. E. Bertrand, P. Chartrand, M. Schaefer, S. M. Shenoy, R. H. Singer, R. M. Long, Localization of ASH1 mRNA particles in living yeast. *Mol. Cell* **2**, 437–445 (1998).

77. M.-T. Wei, Y. C. Chang, S. F. Shimobayashi, Y. Shin, A. R. Strom, C. P. Brangwynne, Nucleated transcriptional condensates amplify gene expression. *Nat. Cell Biol.* **22**, 1187–1196 (2020).

78. S. Leidescher, J. Ribisel, S. Ullrich, Y. Feodorova, E. Hildebrand, A. Galitsyna, S. Bultmann, S. Link, K. Thanisch, C. Mulholland, J. Dekker, K. Leonhardt, L. Mirny, I. Solovei, Spatial organization of transcribed eukaryotic genes. *Nat. Cell Biol.* **24**, 327–339 (2022).

79. H. Kimura, Y. Sato, Imaging transcription elongation dynamics by new technologies unveils the organization of initiation and elongation in transcription factories. *Curr. Opin. Cell Biol.* **74**, 71–79 (2022).

80. S. Uchino, Live imaging of transcription sites using an elongating RNA polymerase II–specific probe. *J. Cell Biol.* **221**, e202104134 (2021).

81. R. Marmorstein, M.-M. Zhou, Writers and readers of histone acetylation: Structure, mechanism, and inhibition. *Cold Spring Harb. Perspect. Biol.* **6**, a018762 (2014).

82. T. Zhang, Z. Zhang, Q. Dong, J. Xiong, B. Zhu, Histone H3K27 acetylation is dispensable for enhancer activity in mouse embryonic stem cells. *Genome Biol.* **21**, 45 (2020).

83. A. Sankar, F. Mohammad, A. K. Sundaramurthy, H. Wang, M. Lerdrup, K. Tatar, K. Helin, Histone editing elucidates the functional roles of H3K27 methylation and acetylation in mammals. *Nat. Genet.* **54**, 754–760 (2022).

84. Q. Jin, L. R. Yu, L. Wang, Z. Zhang, L. H. Kasper, J. E. Lee, C. Wang, P. K. Brindle, S. Y. R. Dent, K. Ge, Distinct roles of GCN5/PCAF-mediated H3K9ac and CBP/p300-mediated H3K18/27ac in nuclear receptor transactivation. *EMBO J.* **30**, 249–262 (2011).

85. C. A. Cialek, G. Galindo, A. L. Koch, M. N. Saxton, T. J. Stasevich, Bead loading proteins and nucleic acids into adherent human cells. *J. Vis. Exp.* **e62559**, (2021).

86. J. Schindelin, I. Arganda-Carreras, E. Frise, V. Kaynig, M. Longair, T. Pietzsch, S. Preibisch, C. Rueden, S. Saalfeld, B. Schmid, J. Y. Tinevez, D. J. White, V. Hartenstein, K. Eliceiri, P. Tomancak, A. Cardona, Fiji: An open-source platform for biological-image analysis. *Nat. Methods* **9**, 676–682 (2012).

87. I. Arganda-Carreras, C. O. S. Sorzano, R. Marabini, J. M. Carazo, C. Ortiz-de-Solorzano, J. Kybic. Consistent and Elastic Registration of Histological Sections Using Vector-Spline

Regularization. in Computer Vision Approaches to Medical Image Analysis (eds. R. R. Beichel & M. Sonka) 85–95 (Springer, 2006).

88. D. Ershov, M. S. Phan, J. W. Pylvänäinen, S. U. Rigaud, L. le Blanc, A. Charles-Orszag, J. R. W. Conway, R. F. Laine, N. H. Roy, D. Bonazzi, G. Duménil, G. Jacquemet, J. Y. Tinevez, TrackMate 7: Integrating state-of-the-art segmentation algorithms into tracking pipelines. *Nat. Methods* **19**, 829–832 (2022).

89. P. Virtanen, SciPy 1.0: Fundamental algorithms for scientific computing in Python. *Nat. Methods* **17**, 261–272 (2020).

90. A. D. Edelstein, M. A. Tsuchida, N. Amodaj, H. Pinkard, R. D. Vale, N. Stuurman, Advanced methods of microscope control using μManager software. *J. Biol. Methods* **1**, e10 (2014).

91. J.-Y. Tinevez, N. Perry, J. Schindelin, G. M. Hoopes, G. D. Reynolds, E. Laplantine, S. Y. Bednarek, S. L. Shorte, K. W. Eliceiri, TrackMate: An open and extensible platform for single-particle tracking. *Methods* **115**, 80–90 (2017).

92. A. V. Weigel, B. Simon, M. M. Tamkun, D. Krapf, Ergodic and nonergodic processes coexist in the plasma membrane as observed by single-molecule tracking. *Proc. Natl. Acad. Sci.* **108**, 6438–6443 (2011).

93. T. Savin, P. S. Doyle, Static and dynamic errors in particle tracking microrheology. *Biophys. J.* **88**, 623–638 (2005).

94. F. Etoc, E. Balloul, C. Vicario, D. Normanno, D. Liße, A. Sittner, J. Piehler, M. Dahan, M. Coppey, Non-specific interactions govern cytosolic diffusion of nanosized objects in mammalian cells. *Nat. Mater.* **17**, 740–746 (2018).